RSC Applied Interfaces

ROYAL SOCIETY OF CHEMISTRY

PAPER

View Article Online
View Journal | View Issue

Cite this: *RSC Appl. Interfaces*, 2025, **2**, 1424

Surface potential-dependent assembly of DNA origami lattices at SiO_2 surfaces†

Adekunle Omoboye,[a] Bhanu Kiran Pothineni,‡[b] Guido Grundmeier,[b] Zhe She [a] and Adrian Keller *[b]

Received 10th June 2025,
Accepted 21st July 2025

DOI: 10.1039/d5lf00169b

rsc.li/RSCApplInter

Self-assembled DNA origami lattices have promising applications in the fabrication of functional surfaces for sensing and plasmonics *via* molecular lithography. While surface-assisted DNA origami lattice assembly at mica surfaces is a straightforward and widely employed method, technologically more relevant SiO_2 surfaces still pose a challenge. Lattice assembly on SiO_2 surfaces is very sensitive toward environmental conditions and surface properties, which often results in comparably low lattice order even under optimized conditions. Here, we investigate DNA origami lattice assembly at oxidized silicon wafers at room temperature with an applied negative substrate potential. *In situ* atomic force microscopy reveals that lattice assembly is notably affected by the applied potential, with −120 mV resulting in the highest lattice order after 120 min incubation. The obtained degree of order, however, is lower than that of lattices assembled under equivalent potential-free conditions at an elevated substrate temperature. Varying the concentrations of monovalent and divalent ions in the electrolyte only leads to a further decrease in lattice order. While our results demonstrate the important role of the surface potential in surface-assisted DNA origami lattice assembly, they also suggest that the achievable degree of lattice order is limited by additional factors such as the roughness of the SiO_2 surfaces.

Introduction

For several decades, DNA has proven to be a reliable molecular building block for the self-assembly of functional materials and nanostructures.[1,2] DNA origami, a widely used technique, is based on folding a long single-stranded DNA scaffold with short DNA oligonucleotides into well-defined shapes.[3–5] Due its ability to produce arbitrarily shaped 2D and 3D nanostructures at high yields, DNA origami has become a common tool in various fields of application, ranging from biosensing[6] and nanomedicine[7] to nanoelectronics[8] and inorganic materials engineering.[9] For instance, DNA origami nanostructures are frequently used as masks in molecular lithography,[10–18] enabling the fabrication of functional surfaces with promising applications as optical metamaterials and sensors.[11,19–21] Real-world applications, however, will additionally require the controlled arrangement of the individual DNA origami nanostructures at the substrate surface. One way to achieve this is the hierarchical self-assembly of DNA origami nanostructures into regular 2D lattices.[22,23]

Among the different methods that can be used to create 2D DNA origami lattices, surface-assisted DNA origami lattice assembly is highly promising for applications in molecular lithography because this method has the ability to fabricate homogenous lattices over macroscopic surface areas of several cm^2.[24] In this method, the quality of the assembled lattice depends critically on the lateral mobility of the adsorbed DNA origami nanostructures and, therefore, on numerous parameters such as the ionic composition of the electrolyte,[25–27] the structural and mechanical properties of the DNA origami nanostructures,[28] and most importantly the substrate material.[25,28,29] Mica surfaces were identified early on as highly suitable substrates for DNA origami lattice assembly[30,31] with the ability to yield astonishingly high lattice order within a few minutes.[26,32] On technologically more relevant SiO_2 surfaces, however, hierarchical assembly of DNA origami lattices was achieved only recently and under very different environmental conditions.[25,28] This is mainly attributed to

[a] *Department of Chemistry, Queen's University, Chernoff Hall, Kingston, ON K7L 3N6, Canada*
[b] *Paderborn University, Technical and Macromolecular Chemistry, Warburger Str. 100, 33098 Paderborn, Germany. E-mail: adrian.keller@uni-paderborn.de*
† Electronic supplementary information (ESI) available: AFM images of the complete time series. See DOI: https://doi.org/10.1039/d5lf00169b
‡ Present address: Programmable Biomaterials Laboratory, Institute of Materials, School of Engineering, École Polytechnique Fédérale de Lausanne, Lausanne 1015, Switzerland.

the fact that SiO_2 in general has a smaller negative zeta potential than mica,[33,34] so that efficient lattice assembly requires much higher concentrations of monovalent cations and elevated substrate temperatures. However, substrate heating leads to convective flows that affect mass transport from the bulk solution to the surface.[35] Furthermore, when an open liquid cell is used, *e.g.*, to enable *in situ* atomic force microscopy (AFM) imaging, the sample solution slowly evaporates during the experiment,[36] which leads to a continuous increase in DNA origami and cation concentrations. Alternative approaches that avoid elevated substrate temperatures would provide better control of the environmental conditions and thus lead to improved reproducibility.

In this work, we attempted to assemble DNA origami lattices at SiO_2 surfaces at room temperature by controlling the surface potential. It was demonstrated by Takabayashi *et al.* that high-fluence boron implantation can be used to tailor the SiO_2 surface potential toward increased DNA origami adsorption at acidic pH values.[37] Here, we followed a more direct approach that has already been employed successfully to control protein adsorption at metal surfaces.[38] In particular, we used p-doped silicon wafers with native surface oxide and polarized the surface oxide during DNA origami adsorption by applying an external negative potential under electrochemical control. DNA origami adsorption and lattice assembly were investigated *in situ* in selected electrolytes by AFM at different potentials. DNA origami lattice assembly was notably affected by the applied potential, with −120 mV resulting in highest lattice order after 120 min incubation, albeit with the overall order being lower than that of lattices assembled under equivalent potential-free conditions at 40 °C. Therefore, while our results demonstrate that the surface potential plays an important role in DNA origami lattice assembly at SiO_2 surfaces, the quality of the formed lattice is influenced also by other factors.

Materials and methods

Substrate preparation

Si(100) wafers (p-doped, 1–10 Ω cm, Siegert Wafer) 2 × 2 cm^2 in size were cleaned in RCA-1 solution (1 : 1 : 5 35% H_2O_2, 25% NH_3, H_2O) for 15 min at 75 °C to remove organic residues and create a hydroxyl-rich surface.

DNA origami assembly

DNA origami triangles[5] were prepared as described previously[32] by folding the 7249 nt M13mp18 scaffold (Tilibit) and 208 staple strands (Eurofins) in 1 × TAE (Carl Roth) supplemented with 10 mM $MgCl_2$ (Carl Roth). The DNA origami triangles were purified by spin filtering using Amicon Ultra 100 K MWCO filters (Millipore). The molar concentration of the purified DNA origami triangles was determined by UV/vis absorption using an Implen Nanophotometer P330.

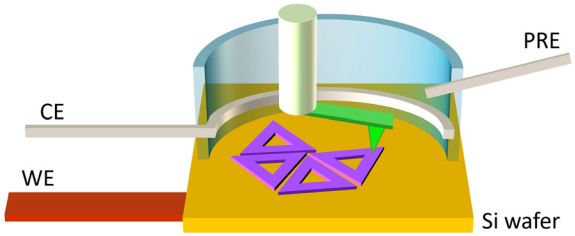

Fig. 1 Schematic representation of the experimental setup. The electrochemical cell (blue) is placed on top of the Si wafer, which acts as the working electrode (WE). The cell houses the platinum counter electrode (CE) and the platinum pseudo-reference electrode (PRE). The AFM cantilever (green) is not used as an electrode.

AFM

AFM measurements were performed using a JPK Nanowizard ULTRA Speed with USC F0.3-k0.3 cantilevers (NanoWorld) and an electrochemical cell (1.5 ml cell volume, JPK). A three-electrode setup was employed (see Fig. 1), comprising the bare silicon wafer with native oxide contacted from the backside as the working electrode (WE), a platinum wire as the counter electrode (CE), and a platinum wire as the pseudo-reference electrode (PRE). This setup was connected to a Gamry Femtostat FAS12 to apply the substrate potentials. For each experiment, 0.5 or 4 nM DNA origami nanostructures were suspended in 1 × TAE (pH 8.5) containing $CaCl_2$ (Merck) and NaCl (VWR) at the desired concentrations. The open circuit potential (OCP) of the substrate in DNA-free electrolyte was recorded before introducing the DNA origami sample solution. The OCP is the potential measured against the PRE when there is no current flowing through the WE. It results from charge separation at the electrode-electrolyte interface and represents the thermodynamic equilibrium of the electrochemical system. After DNA origami injection, a selected potential *vs.* OCP was applied to the WE, *i.e.*, the silicon wafer, in chronoamperometry mode. AFM images were recorded with a scan size of 3 × 3 μm^2, a resolution of 512 × 512 pixels, and a line rate of 3 Hz, resulting in 170 s per frame.

Image analysis

The images were processed using the open-source software Gwyddion[39] to calculate the fast Fourier transforms (FFTs) and the radial power spectral density (PSD) functions. The latter were plotted using OriginPro 2024b and the first correlation peak was fitted with a Lorentzian to determine its full width at half-maximum (fwhm). The determined fwhm was then used to calculate the correlation length ξ of the lattice as described previously.[27] The relative correlation length was obtained by normalizing ξ to the periodicity of the lattice λ. DNA origami surface coverage was determined by applying a suitable height threshold using the Mark by Threshold tool of Gwyddion.[25] The value of the threshold was adjusted individually for each

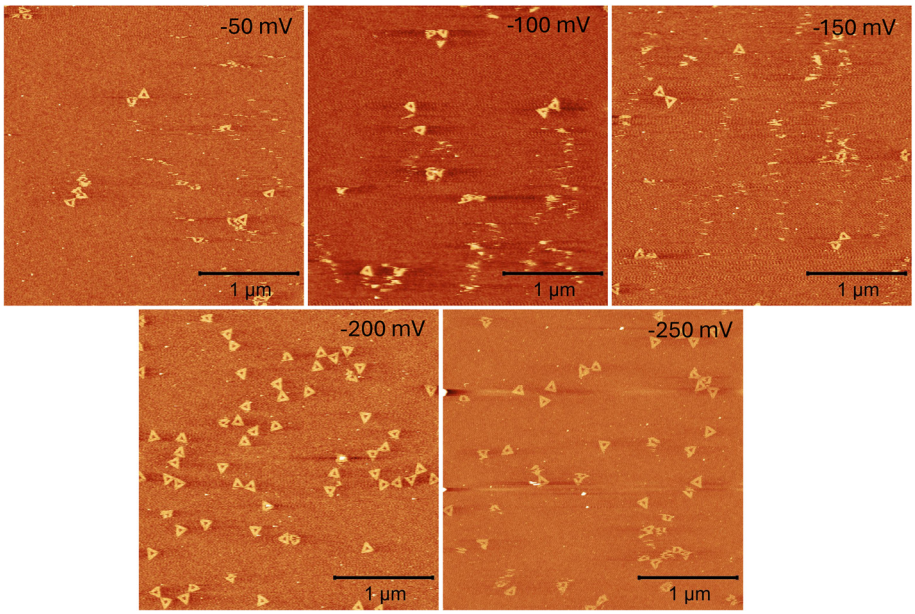

Fig. 2 AFM images (3 × 3 μm^2) of DNA origami triangles at SiO_2 surfaces subjected to different potentials (*vs.* OCP) as indicated. The images were recorded after incubation for 10 to 15 min at 170 s per frame. The applied potential affects the lateral mobility of the adsorbed DNA origami triangles, with higher mobility resulting in blurry shapes and wavy vertical streaks that stem from DNA origami triangles being dragged along during scanning.

image to mask only the DNA origami but not the substrate surface. The surface coverage was then calculated using the Grain Summary tool.

Results and discussion

Effect of the applied potential on DNA origami surface mobility

Before focusing on DNA origami lattice assembly, we first screened the effect of different potentials on the surface mobility of adsorbing DNA origami triangles. For this, we used the same electrolyte conditions that previously resulted in maximum lattice order at an elevated temperature of 40 °C, *i.e.*, 12.5 mM Ca^{2+} and 400 mM Na^+ at pH 8.5.[25] To minimize effects of surface crowding and assess the mobility of single nanostructures, a low DNA origami concentration of 0.5 nM was employed. We started at a potential of −50 mV *vs.* OCP and monitored DNA origami adsorption and diffusion along the surface by *in situ* AFM. In the subsequent experiments, the applied potential was lowered further in −50 mV increments. Fig. 2 shows representative AFM images of DNA origami triangles at the SiO_2 surface with potentials ranging from −50 to −250 mV *vs.* OCP. The images were recorded at 170 s per frame, so that rapidly diffusing DNA origami triangles can be identified by a blurry shape. As can be seen in Fig. 2, this is quite pronounced at potentials between −50 and −150 mV *vs.* OCP, whereas potentials of −200 and −250 mV *vs.* OCP yield well-resolved triangular shapes. The latter is a result of strong DNA origami adsorption with reduced lateral mobility. Since DNA and SiO_2 both are negatively charged at pH 8.5, efficient DNA origami adsorption is facilitated by divalent cations such as Ca^{2+} that cause a charge inversion at the DNA-SiO_2 interface. Replacing some Ca^{2+} ions by Na^+ ions reduces the attractive electrostatic interaction and leads to an increased surface mobility that is required for efficient lattice assembly. Therefore, we can assume that at potentials higher than −200 mV *vs.* OCP, only few Ca^{2+} ions are bound because of either a low affinity for the surface or replacement by Na^+ ions. In this potential range, −150 mV *vs.* OCP seems to lead to a particularly high lateral mobility of the adsorbed DNA origami triangles, as the corresponding image in Fig. 2 shows many wavy vertical streaks that stem from DNA origami triangles being dragged along by the scanning AFM tip. Therefore, we selected the potential range between −100 and −200 mV *vs.* OCP for the following experiments on DNA origami lattice assembly.

Effect of the applied potential on DNA origami lattice assembly

DNA origami lattice assembly in the selected potential range was monitored over a time course of 120 min at a DNA origami concentration of 4 nM that is suitable for efficient lattice formation at elevated temperature.[25] At −100 mV *vs.* OCP, the AFM images in Fig. 3a reveal the slow adsorption of DNA origami triangles over the whole

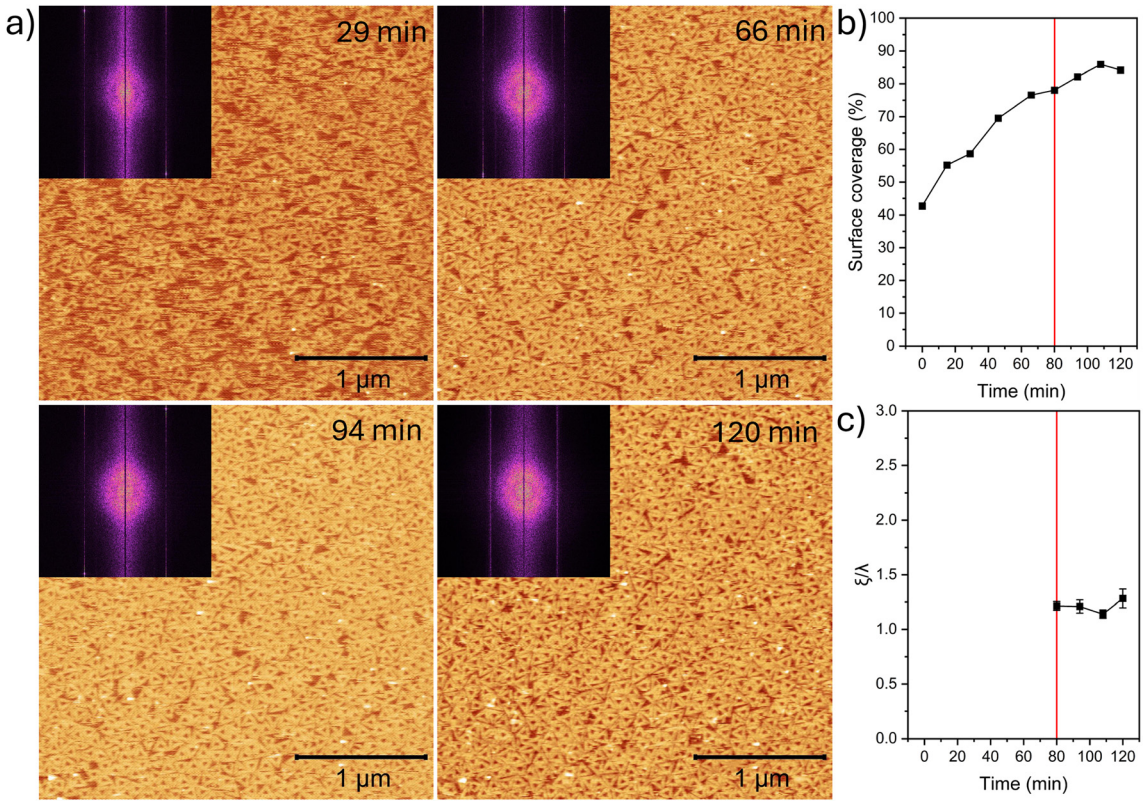

Fig. 3 DNA origami lattice assembly at −100 mV *vs.* OCP. a) AFM images (3 × 3 μm^2) recorded at different time points as indicated. Insets show the FFTs of the images. b) Evolution of surface coverage as determined from the AFM images. c) Evolution of the relative correlation length ξ/λ after formation of a closed monolayer as determined from the PSDs of the AFM images. The red vertical lines in b) and c) indicate the timepoint at which a closed monolayer is observed.

time course. At the early stages of adsorption, the AFM images are rather blurry and have many streaks, which can be attributed to fast DNA origami adsorption and desorption.[27] With increasing incubation time, the surface is getting more densely populated, and image quality improves. The formation of a closed DNA origami monolayer is observed only after incubation for about 80 min (see Fig. 3b). However, the monolayer exhibits many defects in the form of holes, which are only slowly getting filled during further incubation. This is also visible in the evolution of surface coverage in Fig. 3b, which was determined from the AFM images. Here, it can be seen that the surface coverage continues to increase even after monolayer formation.

The development of order in the forming monolayer was assessed *via* Fourier analysis. The FFTs of the recorded AFM images in Fig. 3a have a strong background and only rather faint correlation rings without a discernable hexagonal shape. This does not show notable improvement over time, which is indicative of low lattice order. This was quantified by calculating the relative correlation length ξ/λ, which is a measure of the average size of the single-crystalline domains in the polycrystalline lattice, from the radial PSD functions of the AFM images recorded after monolayer formation (Fig. 3c).[27] The obtained value remains below 1.5, which is significantly lower than that obtained under potential-free conditions at 40 °C, where $\xi/\lambda > 3$ was obtained for incubation times of 120 min and more.[25]

At a potential of −120 mV *vs.* OCP, DNA origami lattice formation is a bit slower than at −100 mV (see Fig. 4a and b) with adsorption and desorption events being less frequent, resulting in improved image quality. Compared to the lower potential, the FFTs of the AFM images show a stronger correlation ring with reduced background, indicating improved lattice order at −120 mV. These features are also reflected in the evolution of the surface coverage and the relative correlation length shown in Fig. 4b and c. The surface coverage increases steadily even after formation of a closed monolayer at about 90 min and does not reach saturation during the experiment. Even though the correlation length again does not increase after a closed monolayer is formed, its value of about 2.5λ is about twice as large as at −100 mV.

Decreasing the applied potential further to −150 mV *vs.* OCP did not result in strong variations in the overall dynamics (see Fig. 5). The most notable difference compared to the previous case of −120 mV *vs.* OCP is the correlation length, which increases from $\xi/\lambda < 1.5$ at the formation of a

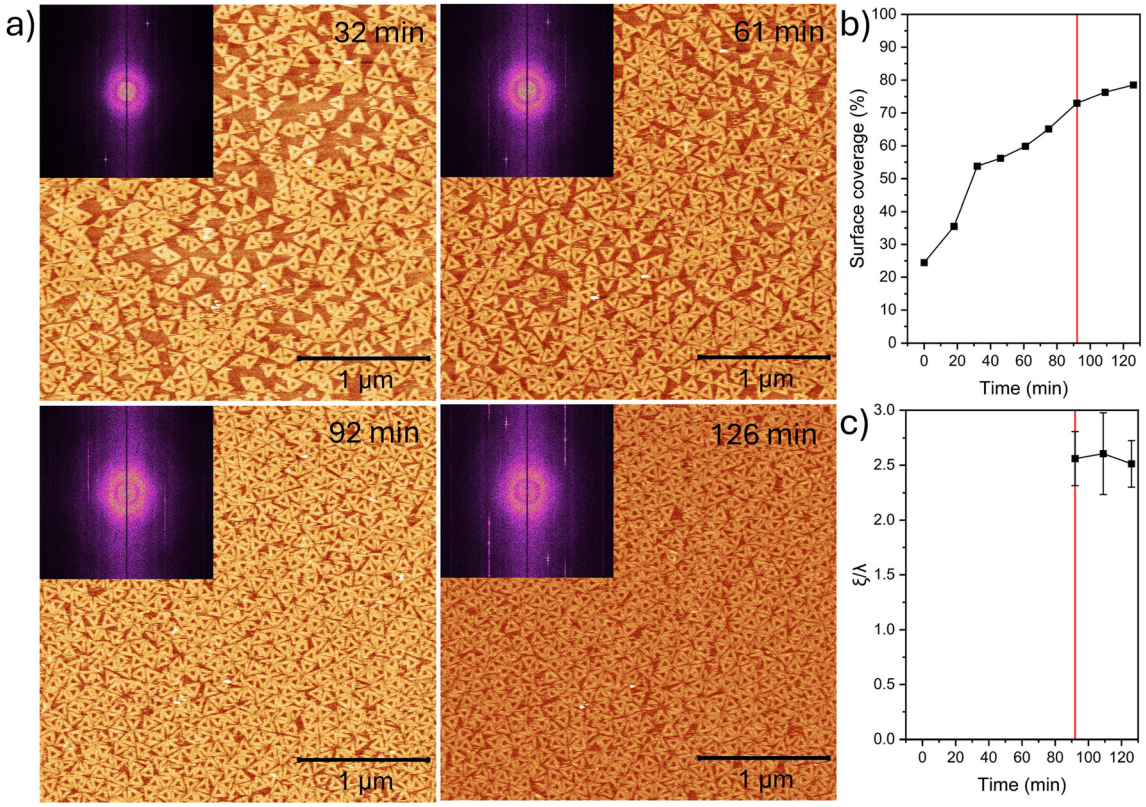

Fig. 4 DNA origami lattice assembly at −120 mV *vs.* OCP. a) AFM images (3 × 3 μm^2) recorded at different time points as indicated. Insets show the FFTs of the images. b) Evolution of surface coverage as determined from the AFM images. c) Evolution of the relative correlation length ξ/λ after formation of a closed monolayer as determined from the PSDs of the AFM images. The red vertical lines in b) and c) indicate the timepoint at which a closed monolayer is observed.

closed monolayer to $\xi/\lambda \sim 2.2$ at the end of the experiment (Fig. 5c).

At an even lower potential of −170 mV *vs.* OCP, the overall situation changes quite dramatically. Here, the SiO_2 surface is densely populated with DNA origami triangles after 25 min, with a closed monolayer forming already after about 40 min of incubation (Fig. 6a and b). This monolayer, however, exhibits many defects and fluctuations due to frequent adsorption and desorption events. This not only has a negative effect on image quality throughout the time course of the experiment but also results in the correlation length remaining at values below 1.5λ (Fig. 6c).

Fig. 7 compares the relative correlation lengths obtained for the different potentials after incubation for about 120 min. The maximum correlation length of about 2.5λ is observed at a potential of −120 mV *vs.* OCP. This value decreases slightly at −150 mV *vs.* OCP. At −100 and −170 mV *vs.* OCP, however, lattice order is much lower at about 1.3λ.

The observed differential effects of the surface potential on DNA origami lattice assembly can be explained by considering potential-dependent cation adsorption at the SiO_2 surface. In general, divalent cations adsorb more readily at charged surfaces than monovalent cations.[40] At small negative potentials (Fig. 8, left), however, adsorption of both cation species at the SiO_2 surface is weak, which results in weak DNA origami adsorption because the electrostatic repulsion between DNA and SiO_2 surface is not fully screened. The resulting high mobility of the adsorbed DNA origami nanostructures leads to a large number of defects in the forming monolayer. Applying more negative potentials (Fig. 8, center) leads to the adsorption of more Ca^{2+} ions, resulting in a partial charge inversion of the SiO_2 surface. Under these conditions, the surface mobility of adsorbing DNA origami nanostructures is reduced, so that a monolayer is formed with fewer lattice defects. At even more negative potentials (Fig. 8, right), the large excess of Na^+ in solution leads to increased Na^+ adsorption at the surface. This in turn decreases the concentration of adsorbed Ca^{2+} ions, which results in an increased mobility of the adsorbed DNA origami nanostructures due to a decreased number of available binding sites. This high mobility hinders lattice formation in the same way as at less negative potentials.

Effect of Na^+ and Ca^{2+} concentrations on DNA origami lattice order

Next, we set out to investigate the influence of the cation concentrations on DNA origami lattice order. For this, we

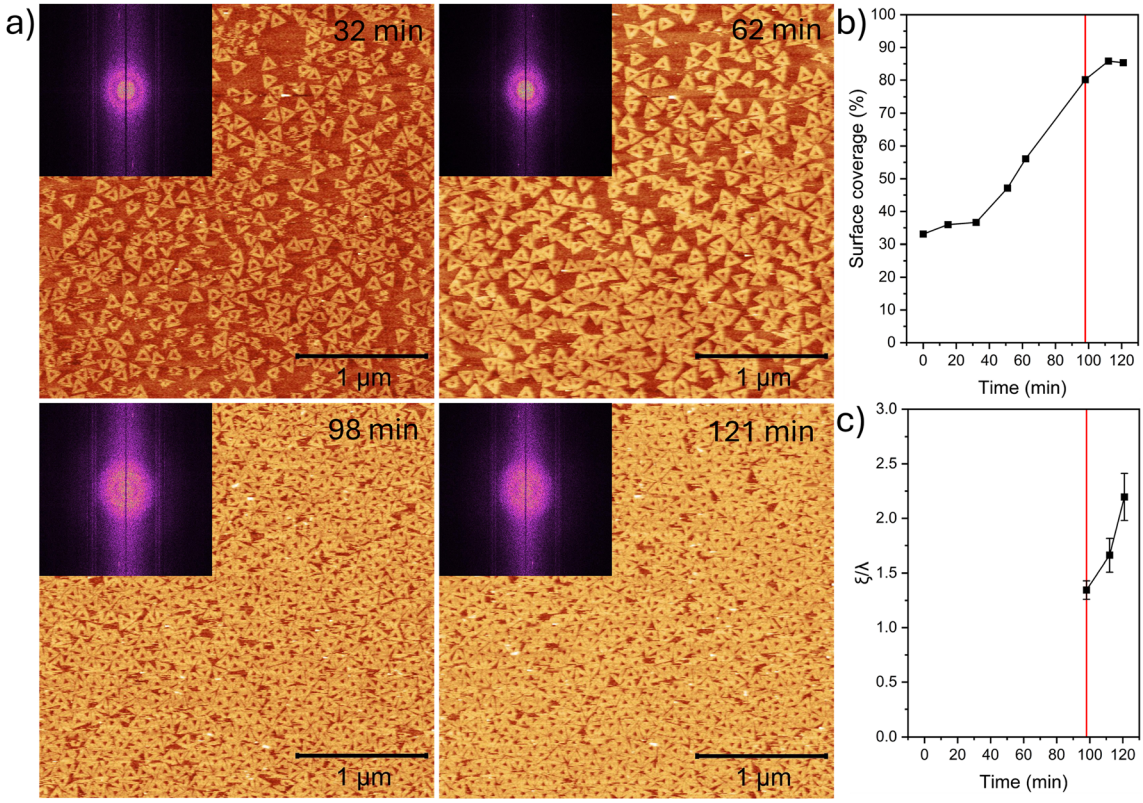

Fig. 5 DNA origami lattice assembly at −150 mV *vs.* OCP. a) AFM images (3 × 3 µm^2) recorded at different time points as indicated. Insets show the FFTs of the images. b) Evolution of surface coverage as determined from the AFM images. c) Evolution of the relative correlation length ξ/λ after formation of a closed monolayer as determined from the PSDs of the AFM images. The red vertical lines in b) and c) indicate the timepoint at which a closed monolayer is observed.

used a potential of −120 mV *vs.* OCP, as this resulted in the highest order in the previous experiments. Fig. 9 shows AFM images of DNA origami triangles incubated at SiO_2 surfaces for about 120 min with different Na^+ concentrations. In the absence of Na^+, no closed monolayer forms within 120 min. At 100 mM Na^+, a closed, densely packed monolayer is observed. The order, however, appears to be rather low, as many of the adsorbed triangles overlap. Consequently, the corresponding FFT is rather blurry and does not show a clear correlation ring. At 600 mM, a densely packed monolayer with increased order is obtained. Based on the FFT, however, it appears to be less ordered than the one obtained at 400 mM (see Fig. 4a). This is verified by the relative correlation lengths plotted in Fig. 9. It is found that the lattice assembled at 600 mM Na^+ has a lower correlation length than the one assembled at 400 mM. The Na^+ concentration dependence at −120 mV thus reflects the one observed in previous experiments at 40 °C, where 400 mM Na^+ led to a higher correlation length after 120 min incubation than 600 mM.[25]

We also evaluated the effect of the Ca^{2+} concentration at a potential of −120 mV *vs.* OCP. As can be seen in Fig. 10, increasing the Ca^{2+} concentration from 12.5 to 15, 17, and 20 mM results in dense yet rather unordered monolayers with different degrees of overlap between the DNA origami triangles. The corresponding plot reveals that for all three concentrations, correlation lengths slightly above 1λ are obtained, which is less than half the value obtained at 12.5 mM.

These experiments demonstrate that for 12.5 mM Ca^{2+} and 400 mM Na^+, maximum lattice order is achieved at a potential of about −120 mV *vs.* OCP and *vice versa*. This indicates an interdependence of the cation concentrations and the applied potential, with other cation concentrations probably requiring different potentials to enable formation of an ordered DNA origami lattice. For the current set of optimized parameters, the degree of order of the obtained lattice as quantified by the relative correlation length is lower than for assembly at 40 °C under otherwise equivalent, potential-free conditions.[25] Specifically, the latter yielded $\xi/\lambda > 3$ for 120 min incubation, whereas the current set of experiments achieved only $\xi/\lambda \sim 2.5$.

Conclusion

In summary, we have investigated the influence of surface potential on the surface-assisted assembly of DNA origami lattices at the native oxide surfaces of silicon wafers. For an electrolyte composition (12.5 mM Ca^{2+} and 400 mM

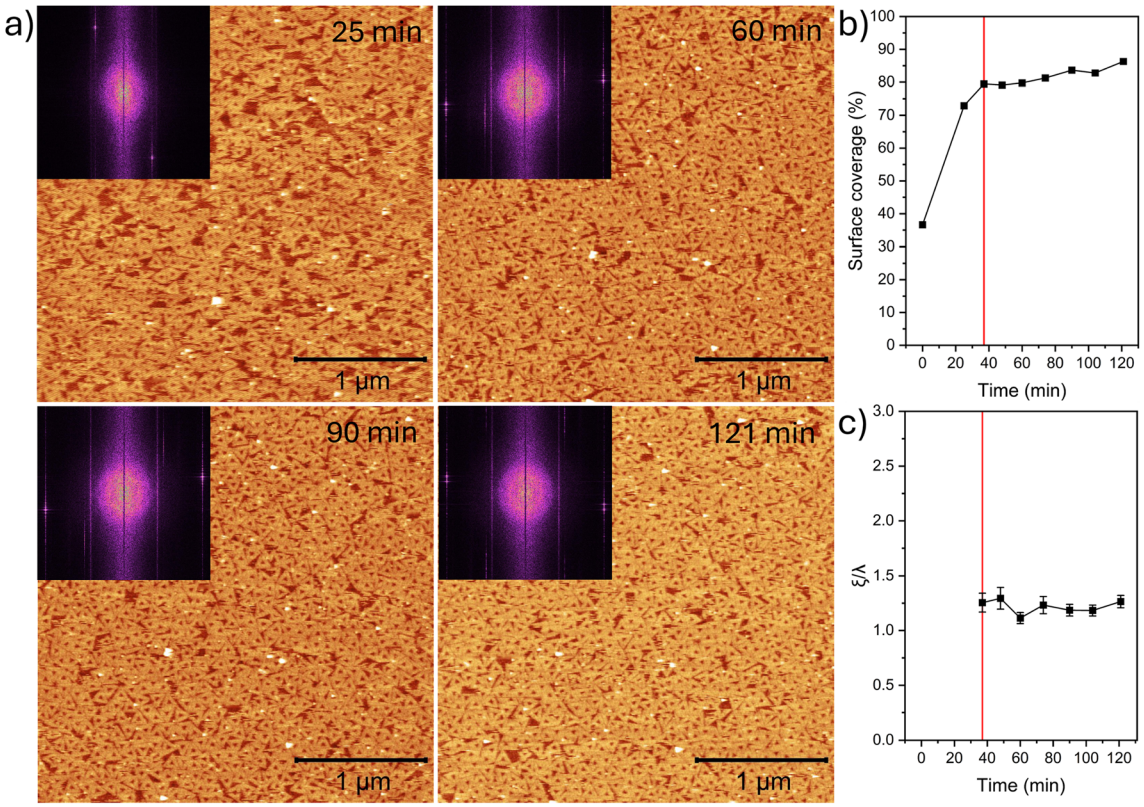

Fig. 6 DNA origami lattice assembly at −170 mV *vs.* OCP. a) AFM images (3 × 3 μm^2) recorded at different time points as indicated. Insets show the FFTs of the images. b) Evolution of surface coverage as determined from the AFM images. c) Evolution of the relative correlation length ξ/λ after formation of a closed monolayer as determined from the PSDs of the AFM images. The red vertical lines in b) and c) indicate the timepoint at which a closed monolayer is observed.

Na^+ in 1 × TAE at pH 8.5) that previously resulted in ordered lattices at elevated temperatures,[25] we found that lattice assembly can be stimulated by applying a potential of −120 mV *vs.* OCP to the substrate. However, the obtained degree of lattice order as quantified by the correlation length of the lattice was found to be worse ($\sim 2.5\lambda$) than that obtained under potential-free conditions at 40 °C ($>3\lambda$). Both higher and lower potentials resulted in even lower lattice order. The same was observed also for variations in the Na^+ and Ca^{2+} concentrations at −120 mV *vs.* OCP. This indicates not only an interdependence of the cation concentrations and the applied potential, but also that the achievable degree of lattice order is limited by a combination of factors. The most obvious one is the surface roughness of the SiO_2 surfaces, which is three to four times larger than that of mica surfaces.[41,42] It was demonstrated recently that a high surface roughness may efficiently suppress DNA origami lattice assembly at SiO_2 surfaces under conditions that resulted in ordered lattices at smoother surfaces.[29] The presence of comparably high surface features may restrict the lateral movement of adsorbed DNA origami nanostructures to such an extent that mobility can be restored only by an elevated substrate temperature. Therefore, future experiments should explore whether an applied substrate potential in combination with an elevated substrate temperature leads to DNA origami lattices of similar quality as those obtained at mica surfaces.

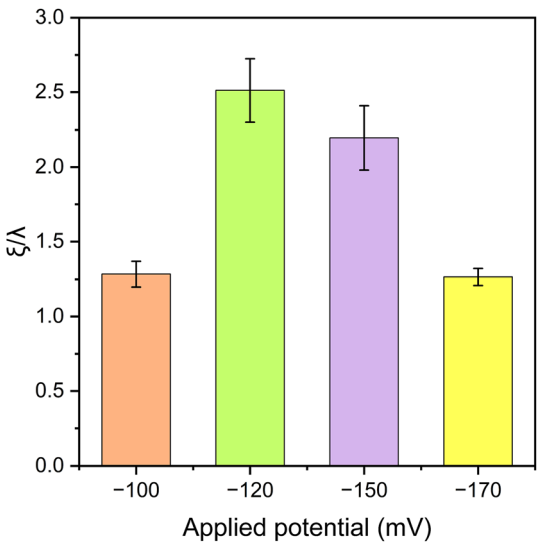

Fig. 7 Relative correlation lengths ξ/λ of the DNA origami lattices assembled for about 120 min at the different potentials (*vs.* OCP).

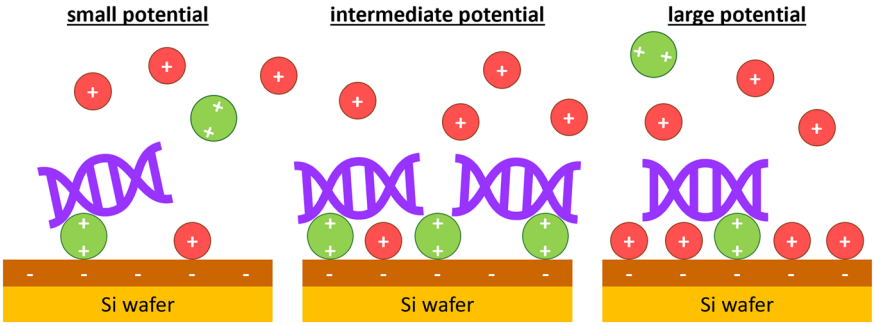

Fig. 8 Schematic representation of the effect of surface potential on cation and DNA origami adsorption. At small negative potentials, only few cations adsorb, resulting in a negative interfacial net charge. Electrostatic repulsion leads to weak DNA origami adsorption. At intermediate negative potentials, Ca^{2+} adsorption results in a positive interfacial net charge, which enables sizable DNA origami adsorption and facilitates lattice assembly. At large negative potentials, adsorbed Ca^{2+} ions are replaced by Na^{+} ions, which are present in large excess. This leads to an almost neutral interface and weak DNA origami adsorption.

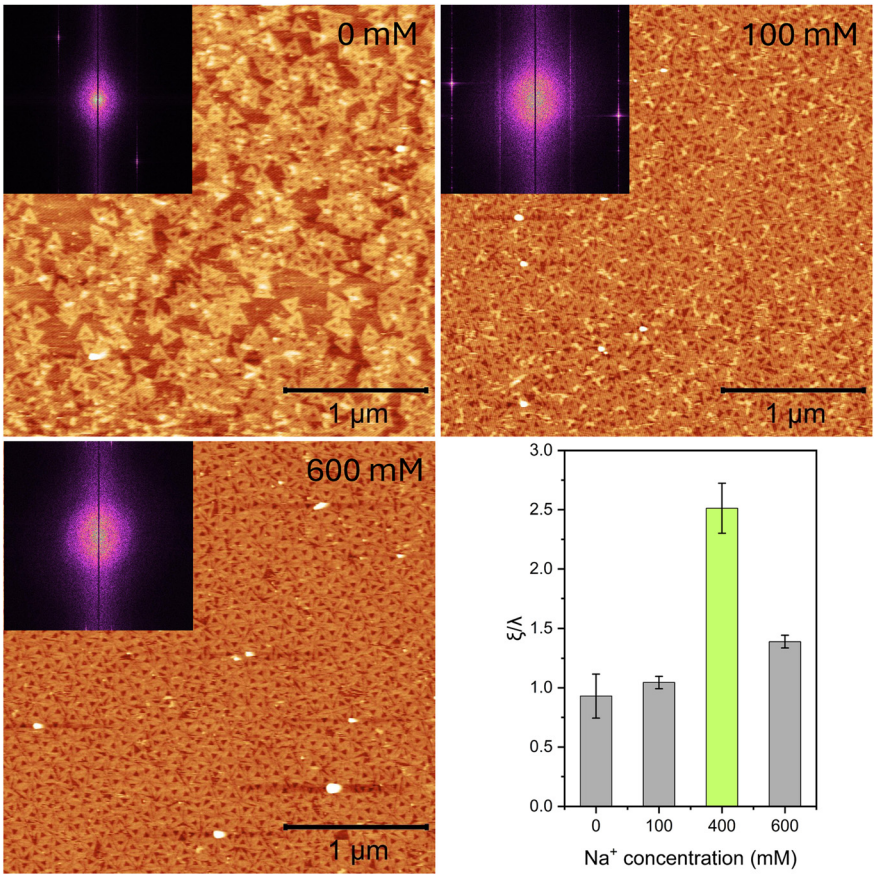

Fig. 9 AFM images (3 × 3 μm^2) recorded after incubation for about 120 min at −120 mV *vs.* OCP in the presence of 12.5 mM Ca^{2+} and different Na^{+} as indicated. Insets show the FFTs of the images. The relative correlation lengths ξ/λ as determined from the PSDs of the AFM images are given in the plot and compared to the maximum value obtained in the previous experiments as shown in Fig. 7 (green).

Finally, we would like to note that although most works in the field so far have focused on enhancing lattice order as much as possible with the ultimate goal of obtaining virtually single-crystalline lattices over macroscopic surface areas, not all applications will require such extreme degrees of order. Some applications may even benefit from lattices with a certain degree of disorder, for instance in the fields of photonic[43] and biomedical[44,45] materials. It will thus depend on the envisioned application of the fabricated lattices whether the experimental challenges and additional costs associated with elevated substrate temperatures are warranted by the achievable improvement in lattice order.

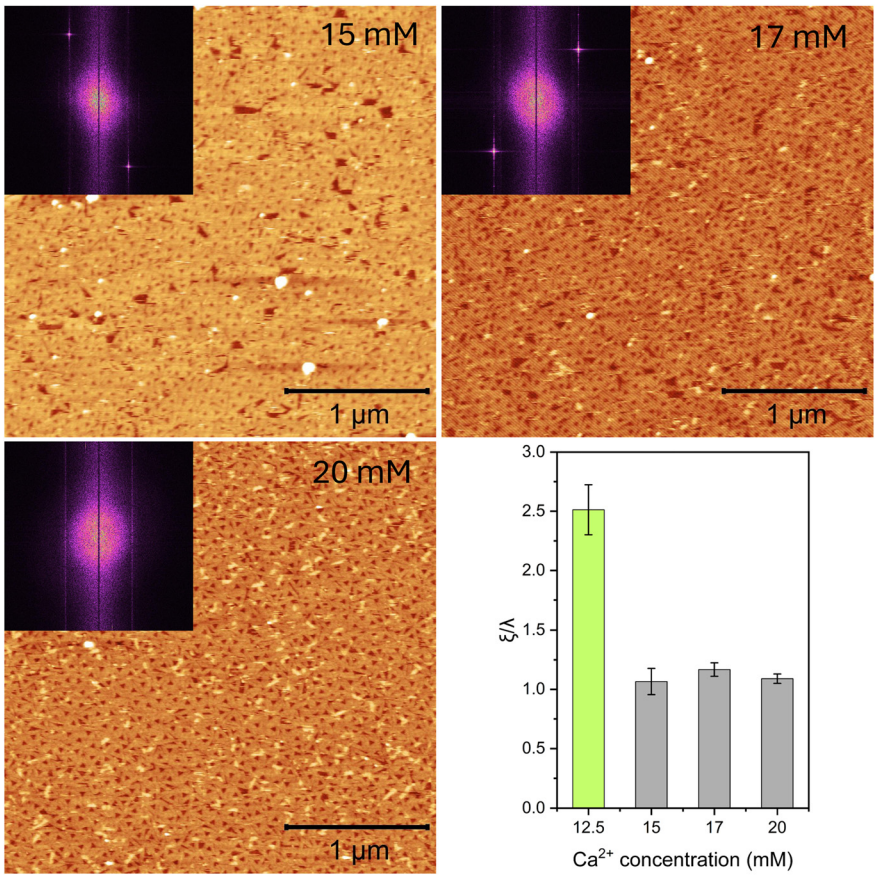

Fig. 10 AFM images (3 × 3 μm^2) recorded after incubation for about 120 min at −120 mV *vs.* OCP in the presence of 400 mM Na^+ and different Ca^{2+} concentrations as indicated. Insets show the FFTs of the images. The relative correlation lengths ξ/λ as determined from the PSDs of the AFM images are given in the plot and compared to the maximum value obtained in the previous experiments as shown in Fig. 7 (green).

Data availability

Data for this article, *i.e.*, raw AFM images, are available at Zenodo at **https://doi.org/10.5281/zenodo.15634927**.

Author contributions

Adekunle Omoboye: formal analysis, funding acquisition, investigation, visualization, writing – original draft, writing – review and editing; Bhanu Kiran Pothineni: formal analysis, investigation, validation, visualization, writing – review and editing; Guido Grundmeier: methodology, resources, writing – review and editing, supervision; Zhe She: funding acquisition, writing – review and editing, supervision; Adrian Keller: conceptualization, funding acquisition, methodology, validation, visualization, writing – review and editing, supervision.

Conflicts of interest

There are no conflicts to declare.

Acknowledgements

We thank C. Ebbert for experimental support. This work was supported by the Deutsche Forschungsgemeinschaft (DFG) under grant number 469036492 (to AK). ZS would like to acknowledge Natural Sciences and Engineering Research Council of Canada (NSERC) for support through the Discovery and Alliance program and the Canada Foundation for Innovation (CFI) for infrastructure support. AO would like to appreciate the Natural Sciences and Engineering Research Council of Canada – Canada Graduate Scholarship Doctoral (NSERC – CGSD), Canada Graduate Scholarships - Michael Smith Foreign Study Supplements (CGS-MSFSS) and Queen's University Faculty of Arts and Science International Research Collaborations Fund.

References

1 A. Heuer-Jungemann and T. Liedl, From DNA Tiles to Functional DNA Materials, *Trends Chem.*, 2019, **1**, 799–814.
2 N. C. Seeman and H. F. Sleiman, DNA nanotechnology, *Nat. Rev. Mater.*, 2018, **3**, 17068.

3 H. Dietz, S. M. Douglas and W. M. Shih, Folding DNA into twisted and curved nanoscale shapes, *Science*, 2009, **325**, 725–730.
4 S. M. Douglas, H. Dietz, T. Liedl, B. Högberg, F. Graf and W. M. Shih, Self-assembly of DNA into nanoscale three-dimensional shapes, *Nature*, 2009, **459**, 414–418.
5 P. W. K. Rothemund, Folding DNA to create nanoscale shapes and patterns, *Nature*, 2006, **440**, 297–302.
6 S. Wang, Z. Zhou, N. Ma, S. Yang, K. Li, C. Teng, Y. Ke and Y. Tian, DNA Origami-Enabled Biosensors, *Sensors*, 2020, **20**, 6899.
7 A. Keller and V. Linko, Challenges and Perspectives of DNA Nanostructures in Biomedicine, *Angew. Chem., Int. Ed.*, 2020, **59**, 15818–15833.
8 L. Hui, R. Bai and H. Liu, DNA-Based Nanofabrication for Nanoelectronics, *Adv. Funct. Mater.*, 2022, **32**, 2112331.
9 A. Heuer-Jungemann and V. Linko, Engineering Inorganic Materials with DNA Nanostructures, *ACS Cent. Sci.*, 2021, **7**, 1969–1979.
10 B. Shen, V. Linko, K. Tapio, M. A. Kostiainen and J. J. Toppari, Custom-Shaped Metal Nanostructures Based on DNA Origami Silhouettes, *Nanoscale*, 2015, **7**, 11267–11272.
11 B. Shen, V. Linko, K. Tapio, S. Pikker, T. Lemma, A. Gopinath, K. V. Gothelf, M. A. Kostiainen and J. J. Toppari, Plasmonic nanostructures through DNA-assisted lithography, *Sci. Adv.*, 2018, **4**, eaap8978.
12 P. Piskunen, B. Shen, A. Keller, J. J. Toppari, M. A. Kostiainen and V. Linko, Biotemplated Lithography of Inorganic Nanostructures (BLIN) for Versatile Patterning of Functional Materials, *ACS Appl. Nano Mater.*, 2021, **4**, 529–538.
13 G. Thomas, C. T. Diagne, X. Baillin, T. Chevolleau, T. Charvolin and R. Tiron, DNA Origami for Silicon Patterning, *ACS Appl. Mater. Interfaces*, 2020, **12**, 36799–36809.
14 L. Hui, R. Nixon, N. Tolman, J. Mukai, R. Bai, R. Wang and H. Liu, Area-Selective Atomic Layer Deposition of Metal Oxides on DNA Nanostructures and Its Applications, *ACS Nano*, 2020, **14**, 13047–13055.
15 S. P. Surwade, S. Zhao and H. Liu, Molecular lithography through DNA-mediated etching and masking of SiO2, *J. Am. Chem. Soc.*, 2011, **133**, 11868–11871.
16 S. P. Surwade, F. Zhou, B. Wei, W. Sun, A. Powell, C. O'Donnell, P. Yin and H. Liu, Nanoscale growth and patterning of inorganic oxides using DNA nanostructure templates, *J. Am. Chem. Soc.*, 2013, **135**, 6778–6781.
17 C. T. Diagne, C. Brun, D. Gasparutto, X. Baillin and R. Tiron, DNA Origami Mask for Sub-Ten-Nanometer Lithography, *ACS Nano*, 2016, **10**, 6458–6463.
18 X. Yuan, D. Xiao, W. Yao, Z. Zhang, L. Yang, L. Zhang, Y. Zeng, J. Liao, S. Luo, C. Li, H. Chen and X. Qu, High-fidelity transfer of area-selective atomic layer deposition grown HfO2 through DNA origami-assisted nanolithography, *Nano Res.*, 2022, **15**, 5687–5694.
19 K. M. Kabusure, P. Piskunen, J. Yang, V. Linko and T. K. Hakala, Raman enhancement in bowtie-shaped aperture-particle hybrid nanostructures fabricated with DNA-assisted lithography, *Nanoscale*, 2023, **15**, 8589–8596.
20 K. M. Kabusure, P. Piskunen, J. Yang, M. Kataja, M. Chacha, S. Ojasalo, B. Shen, T. K. Hakala and V. Linko, Optical characterization of DNA origami-shaped silver nanoparticles created through biotemplated lithography, *Nanoscale*, 2022, **14**, 9648–9654.
21 K. M. Kabusure, P. Piskunen, J. J. Saarinen, V. Linko and T. K. Hakala, Controlling Raman enhancement in particle-aperture hybrid nanostructures by interlayer spacing, *Nanoscale*, 2025, **17**, 3035–3041.
22 S. Julin, A. Keller and V. Linko, Dynamics of DNA Origami Lattices, *Bioconjugate Chem.*, 2023, **34**, 18–29.
23 J. M. Parikka, K. Sokołowska, N. Markešević and J. J. Toppari, Constructing Large 2D Lattices Out of DNA-Tiles, *Molecules*, 2021, **26**, 1502.
24 Y. Xin, B. Shen, M. A. Kostiainen, G. Grundmeier, M. Castro, V. Linko and A. Keller, Scaling Up DNA Origami Lattice Assembly, *Chem. – Eur. J.*, 2021, **27**, 8564–8571.
25 B. K. Pothineni, G. Grundmeier and A. Keller, Cation-dependent assembly of hexagonal DNA origami lattices on SiO2 surfaces, *Nanoscale*, 2023, **15**, 12894–12906.
26 Y. Xin, S. Martinez Rivadeneira, G. Grundmeier, M. Castro and A. Keller, Self-assembly of highly ordered DNA origami lattices at solid-liquid interfaces by controlling cation binding and exchange, *Nano Res.*, 2020, **13**, 3142–3150.
27 C. Kielar, S. Ramakrishnan, S. Fricke, G. Grundmeier and A. Keller, Dynamics of DNA Origami Lattice Formation at Solid-Liquid Interfaces, *ACS Appl. Mater. Interfaces*, 2018, **10**, 44844–44853.
28 K. Tapio, C. Kielar, J. M. Parikka, A. Keller, H. Järvinen, K. Fahmy and J. J. Toppari, Large-Scale Formation of DNA Origami Lattices on Silicon, *Chem. Mater.*, 2023, **35**, 1961–1971.
29 B. K. Pothineni, C. Theile-Rasche, H. Müller, G. Grundmeier, T. de Los Arcos and A. Keller, DNA Origami Adsorption and Lattice Formation on Different SiOx Surfaces, *Chem. – Eur. J.*, 2025, **31**, e202404108.
30 A. Aghebat Rafat, T. Pirzer, M. B. Scheible, A. Kostina and F. C. Simmel, Surface-assisted large-scale ordering of DNA origami tiles, *Angew. Chem., Int. Ed.*, 2014, **53**, 7665–7668.
31 S. Woo and P. W. K. Rothemund, Self-assembly of two-dimensional DNA origami lattices using cation-controlled surface diffusion, *Nat. Commun.*, 2014, **5**, 4889.
32 B. K. Pothineni, J. Barner, G. Grundmeier, D. Contreras, M. Castro and A. Keller, Rapid assembly of highly ordered DNA origami lattices at mica surfaces, *Discover Nano*, 2025, **20**, 77.
33 L. Bousse, S. Mostarshed, B. van der Shoot, N. de Rooij, P. Gimmel and W. Göpel, Zeta potential measurements of Ta2O5 and SiO2 thin films, *J. Colloid Interface Sci.*, 1991, **147**, 22–32.
34 P. J. Sides, D. Faruqui and A. J. Gellman, Dynamics of charging of muscovite mica: measurement and modeling, *Langmuir*, 2009, **25**, 1475–1481.

35 M. I. Pividori and S. Alegret, in *Immobilisation of DNA on Chips I*, ed. C. Wittmann, Springer-Verlag, Berlin/Heidelberg, 2005, pp. 1–36.
36 J. Parikka, B. K. Pothineni, H. Järvinen, K. Tapio, A. Keller and J. J. Toppari, Surface-Assisted Assembly of DNA Origami Lattices on Silicon Wafers, *Methods Mol. Biol.*, 2025, **2901**, 89–101.
37 S. Takabayashi, S. Kotani, J. Flores-Estrada, E. Spears, J. E. Padilla, L. C. Godwin, E. Graugnard, W. Kuang, S. Sills and W. L. Hughes, Boron-Implanted Silicon Substrates for Physical Adsorption of DNA Origami, *Int. J. Mol. Sci.*, 2018, **19**, 2513.
38 B. Duderija, A. González-Orive, C. Ebbert, V. Neßlinger, A. Keller and G. Grundmeier, Electrode Potential-Dependent Studies of Protein Adsorption on Ti6Al4V Alloy, *Molecules*, 2023, **28**, 5109.
39 D. Nečas and P. Klapetek, Gwyddion: an open-source software for SPM data analysis, *Open Phys.*, 2012, **10**, 181–188.
40 M. Valiskó, D. Boda and D. Gillespie, Selective Adsorption of Ions with Different Diameter and Valence at Highly Charged Interfaces, *J. Phys. Chem. C*, 2007, **111**, 15575–15585.
41 A. Keller, M. Fritzsche, R. Ogaki, I. Bald, S. Facsko, M. Dong, P. Kingshott and F. Besenbacher, Tuning the hydrophobicity of mica surfaces by hyperthermal Ar ion irradiation, *J. Chem. Phys.*, 2011, **134**, 104705.
42 Y. Yang, M. Yu, F. Böke, Q. Qin, R. Hübner, S. Knust, S. Schwiderek, G. Grundmeier, H. Fischer and A. Keller, Effect of nanoscale surface topography on the adsorption of globular proteins, *Appl. Surf. Sci.*, 2021, **535**, 147671.
43 S. Yu, C.-W. Qiu, Y. Chong, S. Torquato and N. Park, Engineered disorder in photonics, *Nat. Rev. Mater.*, 2021, **6**, 226–243.
44 M. J. Dalby, N. Gadegaard, R. Tare, A. Andar, M. O. Riehle, P. Herzyk, C. D. W. Wilkinson and R. O. C. Oreffo, The control of human mesenchymal cell differentiation using nanoscale symmetry and disorder, *Nat. Mater.*, 2007, **6**, 997–1003.
45 J. Huang, S. V. Grater, F. Corbellini, S. Rinck, E. Bock, R. Kemkemer, H. Kessler, J. Ding and J. P. Spatz, Impact of order and disorder in RGD nanopatterns on cell adhesion, *Nano Lett.*, 2009, **9**, 1111–1116.